Combustion modeling study for a GCH4/GOX single element combustion chamber: unsteady simulations

By H. Terashi† AND Yu Daimon‡,

University of Tokyo, 2-11-16 Yayoi, Bunkyo, Tokyo, Japan
‡Japan Aerospace Exploration Agency, 2-1-1 Sengen, Tsukuba, Ibaraki, Japan

1. Introduction

Large-eddy simulations (LES) or direct numerical simulations (DNS) have been considered a more attractive approach than Reynolds-averaged Navier-Stokes simulations (RANS) for the prediction of unsteady flow features. In addition to the RANS simulations, we have performed a two-dimensional (2-D) DNS for the combustion flow fields of a GOX/GCH_4 single injector, while introducing a detailed chemical kinetic mechanism for resolving an interaction between unsteady fluid dynamics and chemical reactions. The detailed unsteady flow structures obtained during the summer program are presented below.

2. Numerical method

2.1. *Governing equations*

The governing equations are the two-dimensional Navier-Stokes equations with the mass conservation equations of each chemical species in a curvilinear coordinate system and a thermally perfect gas is assumed, which are written as follows:

$$\frac{\partial \rho}{\partial t} + \nabla \cdot (\rho \boldsymbol{u}) = 0, \tag{2.1}$$

$$\frac{\partial (\rho \boldsymbol{u})}{\partial t} + \nabla \cdot (\rho \boldsymbol{u} \otimes \boldsymbol{u} + p\boldsymbol{\delta} - \boldsymbol{\tau}) = 0, \tag{2.2}$$

$$\frac{\partial E}{\partial t} + \nabla \cdot [(E+p)\boldsymbol{u} - \boldsymbol{\tau} \cdot \boldsymbol{u} + \boldsymbol{q}] = 0, \tag{2.3}$$

$$\frac{\partial (\rho Y_s)}{\partial t} + \nabla \cdot (\rho Y_s \boldsymbol{u} - \rho D_s \nabla Y_s) = \dot{\omega}_s, \tag{2.4}$$

$$p = \rho R \sum_{s=1}^{N} \frac{Y_s}{M_s} T, \tag{2.5}$$

where ρ is the density, $\boldsymbol{u}$ is the velocity vector, p is the pressure, $\boldsymbol{\delta}$ is the unit tensor, $\boldsymbol{\tau}$ is the viscous stress tensor, E is the total energy ($E = \rho e + \frac{1}{2}\rho \boldsymbol{u} \cdot \boldsymbol{u}$), $\boldsymbol{q}$ is the heat flux vector, e is the internal energy, Y_s is the mass fraction, D_s is the diffusion coefficient, $\dot{\omega}_s$ is the production rate of each species s. R is the universal gas constant ($R = 8.314$ J mol^{-1} K^{-1}), T is the temperature, and M_s is the molar mass of each species. Here the subscript $s = 1 \sim N$ where N is the total number of species.

† mahtera@rocketlab.t.u-tokyo.ac.jp

The single component viscosities and binary diffusion coefficients are calculated by the standard kinetic theory expression of Hirschfelder [1], and the single component thermal conductivities are calculated by Warnatz's model [2]. For mixtures, the thermal conductivity is modeled with the formula of Mathur et al. [3], and analogous to the thermal conductivity, the mixture-averaged viscosity is purposely modeled with an empirical approximation [4] for the low computational cost. The mixture diffusion coefficient D_s is given by a mixture-averaged model based on Fick's Law [5, 6]. The Dufour effect for the heat flux, the Soret effect and the pressure diffusion for the diffusion flux are neglected in this study.

The fluid and chemical reaction parts in the governing equations are solved separately in the time integration. The fluid parts in Eqs. (2.1) – (2.4) are integrated under the assumption that the chemical reactions are frozen, $\dot{\omega}_s = 0$ in Eq. (2.4), whereas the chemical reaction parts are treated under the assumption that the volume and internal energy of fluids are constant. Thus, the governing equations for the chemical reactions are derived as follows:

$$\rho \frac{\mathrm{d}Y_s}{\mathrm{d}t} = \dot{\omega}_s, \tag{2.6}$$

$$\rho c_v \frac{\mathrm{d}T}{\mathrm{d}t} = -\sum_{s=1}^{N} e_s \dot{\omega}_s, \tag{2.7}$$

where e_s is the internal energy of each species and c_v is the specific heats at a constant volume. The spatial derivatives in Eqs. (2.1) – (2.4) are neglected in the chemical reaction part.

CHEMKIN-II libraries [7, 8] are used to evaluate the variables related to thermodynamics, transports, and chemical reactions. Primitive variables such as the temperature, mass fractions, and pressure are exchanged between the fluid equations (2.1) – (2.4) and the chemical reaction equations (2.6) and (2.7) at each time step.

2.2. *Numerical methods for the fluid part*

For the Navier–Stokes equations without chemical reaction terms, the numerical flux is evaluated using the Harten–Lax–van Leer–Contact scheme [9] with a modification [10]. Higher-order spatial accuracy is achieved using the Monotone Upstream Centered Schemes for Conservation Law with primitive variable interpolation and a minmod limiter [11]. Velocity reconstruction by Thornber et al. [12] is applied to the reduce numerical dissipation introduced by low Mach number features. The viscous, heat conductivity, and diffusion terms are evaluated by the second-order central differencing. The time integration is performed with the third-order total variation diminishing Runge–Kutta scheme [13]. In this study, no sub-grid scale model is used, i.e., the coupling between the fluid and chemical reaction terms is expected to be resolved with computational grids.

2.3. *Numerical method for the chemical reaction part*

A robust and fast explicit time integration method [14] is used to efficiently conduct the time integration of the reaction equations (2.6) and (2.7) while overcoming possible stiffness. The method is based on a quasi-steady-state assumption and a general formula that preserves conservation laws for any integration operator. The performance and accuracy have been comprehensively validated with zero-dimensional ignition problems

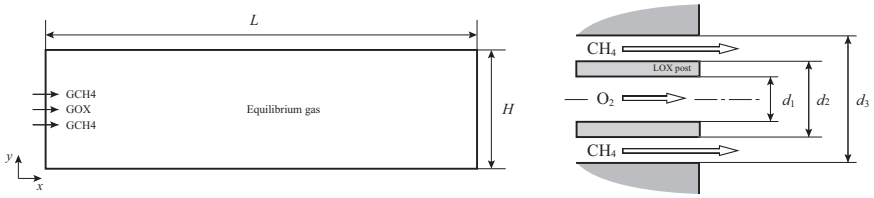

(a) Computational domain (b) Injector

FIGURE 1. Schematic of dimensions for injector and computational domain (not to scale)

	mm
GOX internal diameter, d_1	4
GCH_4 internal diameter, d_2	5
GCH_4 external diameter, d_3	6
GOX post wall thickness	0.5
Domain hight, H	12
Domain length, L	250

TABLE 1. Dimensions for injector and computational domain.

under various conditions [14]. These numerical techniques have been successfully applied to various compressible reactive flow simulations [15–17].

3. Computational conditions

In this study, a two-dimensional (2-D) rectangular domain without a nozzle or injector is considered, which is reduced from the original three-dimensional (3-D) combustion chamber geometry. As shown in Fig. 1, gaseous oxygen is injected from the inner tube, which is surrounded by gaseous methane injected from the outer tube. Table. 1 shows the dimensions for the injector and computational domain shown in Fig. 1.

The chamber pressure is set to 2 MPa as a target combustion pressure. It is assumed that the chamber is initially filled with the equilibrium gas, which is determined using NASA-CEA2 [18] with a stoichiometric condition for methane/oxygen and a temperature of 300 K at constant pressure and enthalpy. The high-temperature equilibrium gas initiates the ignition of methane/oxygen injected into the chamber. The injection conditions are presented in Table. 2. The injection velocity is obtained from a preliminary result using a RANS simulation, in which the complete 3-D geometry of the injector and chamber is simulated. An adiabatic wall is assumed with a non-slip velocity condition for the inlet, upper and lower walls, although it is not expected that the wall boundary layer is fully resolved by the computational grids used in this study. A non-reflecting boundary condition [19, 20] with a mean pressure of 2 MPa is applied to the outlet boundary.

The baseline grid used in the following discussion consists of 607×481 grid points with a minimum grid spacing Δs_{min} of approximately 25 μm. Note that a grid convergence study preliminarily conducted with four different minimum grid resolutions ranging from 18 to 50 μm demonstrates that the baseline grid resolution is sufficient for resolving combustion flow features such as methane/oxygen non-premixed flame dynamics or

	p, MPa	T, K	u, m/s
GOX for inner jet	2	300	150
GCH_4 for outer jet	2	300	170

TABLE 2. Injection conditions.

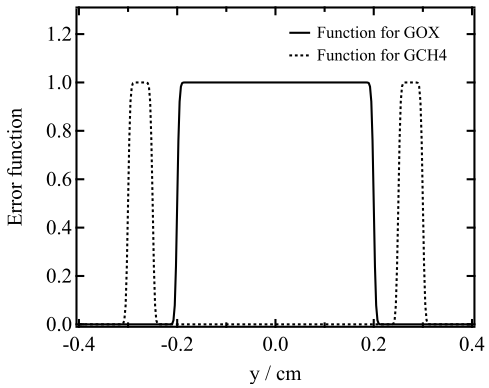

FIGURE 2. Error functions with $C_\epsilon = 2$ used for the inlet profiles.

quenching behaviors discussed in the following section. The Courant-Friedrich-Lewy number is set to 0.6, which corresponds to a physical time step size of approximately 1×10^{-8} s with a minimum grid spacing of 25 μm.

The profiles of pressure, temperature, and mass fractions of species at the inlet are smoothly generated in the y direction using an error function,

$$f(\Delta h) = \mathrm{erf}\left(\Delta h/(C_\epsilon \Delta s_{min})\right), \tag{3.1}$$

where Δh is the distance from the center of the GOX jet and C_ϵ is the adjustable parameter $C_\epsilon = 2.0$ is used unless otherwise noted. An example of the error function at the inlet is shown in Fig. 2. The present study also uses an adjustable parameter of $C_\epsilon = 0.0$, i.e., a flat inlet profile, to investigate the effects of inlet profiles on combustion flow fields, which is discussed later.

A detailed reaction mechanism of methane, which consists of 33 species and 150 reactions, is used for calculating the reaction rate in eq. (2.4). The present mechanism is carefully reduced by DRG [21] from the original one of 68 species and 334 reactions generated by KUCRS [22], and it has been thoroughly confirmed that prediction accuracies for ignition delay and the laminar flame velocity are almost identical to those of the original mechanism under various conditions.

4. Results

4.1. *Overall combustion flow fields*

Figure 3 shows an instantaneous combustion flow field with the temperature and mass fractions of CH_4 and O_2. Non-premixed flames are generated between CH_4 and O_2 and are initiated by the presence of high-temperature equilibrium gas that initially occupies

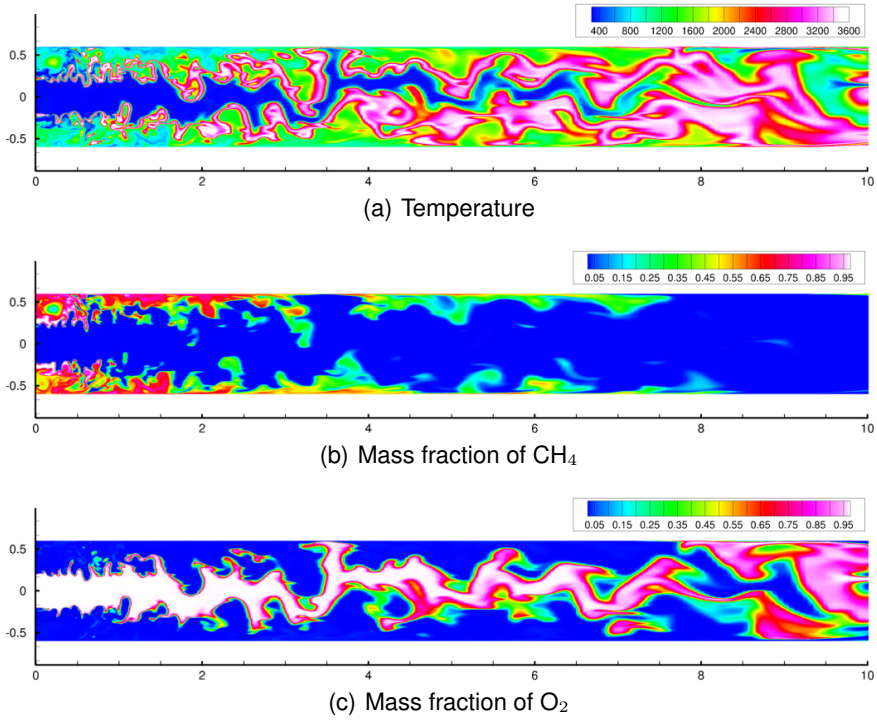

(a) Temperature

(b) Mass fraction of CH_4

(c) Mass fraction of O_2

FIGURE 3. Instantaneous combustion flow fields at $t = 8.071 \times 10^{-4}$ s from the injection.

the chamber. Two large recirculation regions are established in the upper and lower corners near the injector inlet, in which non-premixed flames and unburnt CH_4 are captured and introduced. Hence, a high-temperature recirculation region is established in the corner, along with an enhanced rate of thermal decomposition of the unburnt CH_4 (see Fig. 3(b)), which is generally difficult to simulate using RANS assumptions. Strong unsteadiness is only observed in the recirculation regions near the injector inlet between $x = 0.0$ and 2.0, while high-temperature burnt gases steadily flow through in the downstream region. Thus, the discussion below is focused on detailed flow structures near the injector inlet.

4.2. *Detailed unsteady behavior near the injector*

Figures 4(a) and 4(b) show two views of the temperature distributions, while highlighting detailed unsteady behaviors near the injector inlet. It is shown that the non-premixed flames between the CH_4 and O_2 jets are initiated in the recirculation regions formed behind the LOX posts, to which unburnt CH_4 and O_2 are steadily supplied. While the non-premixed flames are continuously generated behind the LOX posts, the flames in the downstream region split intermittently like vortex shedding phenomena behind a cylinder. This is mainly caused by unsteady behavior, not just from the jet instability but also from the recirculation flow in the corner. The mass fraction of CH_4 in Fig. 4(c) demonstrates that most of the CH_4 jet is captured and introduced into the recirculation region in the corner, and the rest of the CH_4 flows along the walls towards the downstream region. Since the flames between the CH_4 and O_2 jets exist stably under the

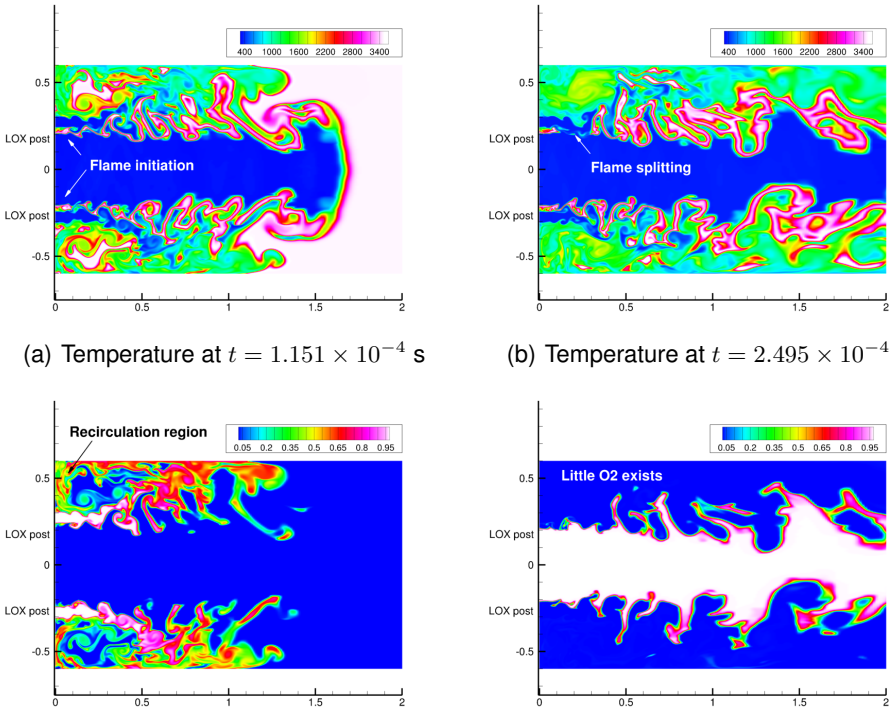

(a) Temperature at $t = 1.151 \times 10^{-4}$ s (b) Temperature at $t = 2.495 \times 10^{-4}$ s

(c) Mass fraction of CH_4 at $t = 2.495 \times 10^{-4}$ s (d) Mass fraction of O_2 at $t = 2.495 \times 10^{-4}$ s

FIGURE 4. Representative contours in a stable combustion case.

present conditions, it is confirmed in Fig. 4(d) that the majority of the O_2 jet is naturally used in flame generation and therefore little O_2 leaks into the upper and lower regions.

4.3. *Unstable combustion mode*

While stable combustion is observed under the current conditions, an additional simulation was also performed to investigate the effects of inlet conditions on combustion flow fields of a coaxial-type injector. Here a sharp profile is intentionally generated at the inlet with an adjustable parameter of $C_\epsilon = 0.0$, in order to assume the jet injection with a very thin boundary layer. Only the inlet profile is modified, while the other conditions are kept the same as in the previous simulation.

Figure 5 shows a sequential view of the temperature distribution near the injector inlet. Although the non-premixed flames are initially generated between the CH_4 and O_2 jets, it is shown in Fig. 5(b) that the lower flame behind the LOX post first disappears followed by the disappearance of the upper flame in Fig. 5(c). Once the flames disappear, some of unburnt O_2 jets are able to mix with unburnt CH_4 in a low-temperature state due to the absence of high-temperature flames. As a result, the premixed CH_4/O_2 gases are partly produced in the combustion chamber. Since these premixed CH_4/O_2 gases are surrounded by high-temperature gases initially generated and captured in the recirculation region in the corner, autoignition of the premixed gases eventually takes place at several locations with certain ignition delay times, possibly generating strong pressure waves in the combustion chamber. Thus, as shown in Fig. 5(d), the resulting combustion

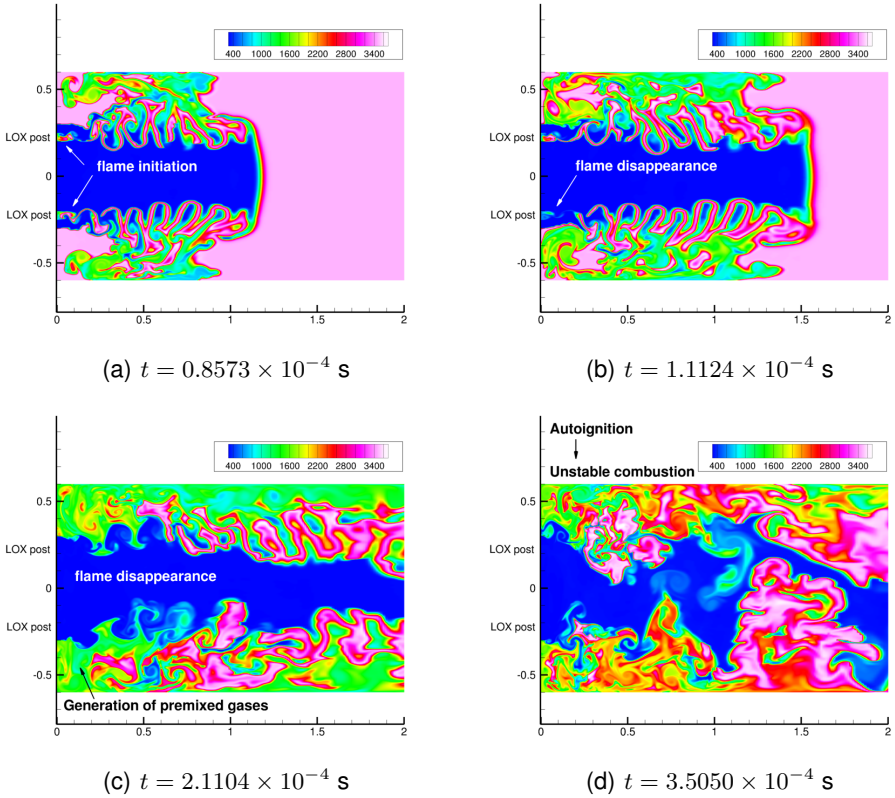

(a) $t = 0.8573 \times 10^{-4}$ s

(b) $t = 1.1124 \times 10^{-4}$ s

(c) $t = 2.1104 \times 10^{-4}$ s

(d) $t = 3.5050 \times 10^{-4}$ s

FIGURE 5. A sequential view of temperature distributions in an unstable combustion case.

flow field seems very unstable and fluctuating compared to the previous one, although quantitative analysis is required. Nevertheless, the present result indicates that, in a coaxial-type injector system, the disappearance of non-premixed flames between the fuel and oxidizer can be a trigger for an unstable combustion mode through the production of premixed gases and autoignition. At this point, although the detailed mechanism behind the disappearance of the flames remains unclear, it seems that strong mixing due to the sharp inlet profile, i.e., the thin boundary layer, induces much incursion of the low-temperature jets into the recirculation region behind the LOX post, which weakens the flame sustainability in the recirculation region.

5. Conclusions

A 2-D DNS simulation is performed for a CH_4/O_2 coaxial injector using detailed chemical kinetics with the compressible Navier-Stokes equations, where the fluid dynamics and chemical kinetics are fully coupled. The result shows that the relatively high-temperature and CH_4-rich recirculation region is established in the upper and lower corners, unlike in the case of the RANS simulations. The result, with a sharp inlet profile, interestingly shows the generation of an unstable combustion mode, which is not observed with a smooth inlet profile and RANS simulations. It is shown that the disappearance of non-premixed flames behind the LOX post is a trigger for the unstable

combustion mode through the production of partly premixed gases and the generation of autoignition at several locations in the combustion chamber. The resultant combustion flow field is very unstable and fluctuating. The disappearance of the flames may be caused by strong mixing in the recirculation region behind the LOX post due to the sharp inlet profile.

Acknowledgments

Financial support has been provided by the German Research Foundation (Deutsche Forschungsgemeinschaft – DFG) in the framework of the Sonderforschungsbereich Transregio 40.

References

[1] J. HIRSCHFELDER, C. CURTISS, R. BIRD, *Molecular theory of gases and liquids*, John Wiley and Sons, Inc., New York, 1954.

[2] N. PETERS, J. WARNATZ, Numerical methods in laminar flame propagation: A GAMM-Workshop, Vol. 6, Informatica International, Inc., 1982.

[3] S. MATHUR, P. TONDON, S. SAXENA, Thermal conductivity of binary, ternary and quaternary mixtures of rare gases, *Molecular Physics* 12 (6) (1967) 569–579.

[4] J. WARNATZ, U. MAAS, R. W. DIBBLE, *Combustion: physical and chemical fundamentals, modeling and simulation, experiments, pollutant formation*, Springer, 2006.

[5] R. B. BIRD, W. E. STEWART, E. N. LIGHTFOOT, *Transport phenomena*, Vol. 2, Wiley New York, 1960.

[6] K. SUTTON, P. A. GNOFFO, Multi-component diffusion with application to computational aerothermodynamics, in: Proceedings of 7th AIAA/ASME Joint Thermophysics and Heat Transfer Conference, AIAA98-2575, 1998.

[7] R. KEE, F. RUPLY, J. MILLER, Chemkin-II: A fortran chemical kinetics package for the analysis of gas-phase chemical kinetics, Sandia Report SAND89-8009 (1989).

[8] R. KEE, G. DIXON-LEWIS, J. WARNATZ, M. COLTRIN, J. MILLER, A fortran computer code package for the evaluation of gas-phase, multicomponent transport properties, SAND86-8246 (1986).

[9] E. F. TORO, M. SPRUCE, W. SPEARES, Restoration of the contact surface in the HLL-Riemann solver, *Shock Waves* 4 (1) (1994) 25–34.

[10] S. D. KIM, B. J. LEE, H. J. LEE, I.-S. JEUNG, Robust HLLC Riemann solver with weighted average flux scheme for strong shock, *Journal of Computational Physics* 228 (20) (2009) 7634–7642.

[11] B. VAN LEER, *Flux-vector splitting for the Euler equation*, Springer, 1997.

[12] B. THORNBER, A. MOSEDALE, D. DRIKAKIS, D. YOUNGS, R. J. WILLIAMS, An improved reconstruction method for compressible flows with low mach number features, *Journal of Computational Physics* 227 (10) (2008) 4873–4894.

[13] S. GOTTLIEB, C.-W. SHU, Total variation diminishing Runge-Kutta schemes, *Mathematics of Computation of the American Mathematical Society* 67 (221) (1998) 73–85.

[14] Y. MORII, H. TERASHIMA, M. KOSHI, T. SHIMIZU, E. SHIMA, Fast and robust time integration method for stiff chemical kinetic ODEs, in: Proceedings of AIAA Propulsion and Energy Forum and Exposition 2014, AIAA2014-3920, 2014.

[15] H. TERASHIMA, M. KOSHI, C. MIWADA, T. MOGI, R. DOBASHI, Effects of initial diaphragm shape on spontaneous ignition of high-pressure hydrogen in a two-dimensional duct, *International Journal of Hydrogen Energy* 39 (11) (2014) 6013–6023.

[16] H. TANI, H. TERASHIMA, M. KOSHI, Y. DAIMON, Hypergolic ignition and flame structures of hydrazine/nitrogen tetroxide co-flowing plane jets, Proceedings of the Combustion Institute 35 (2) (2015) 2199–2206.

[17] H. TERASHIMA, M. KOSHI, Mechanisms of strong pressure wave generation in end-gas autoignition during knocking combustion,*Combustion and Flame* 162 (5) (2015) 1944–1956.

[18] B. J. MCBRIDE, S. GORDON, Computer program for calculation of complex chemical equilibrium compositions and applications: II. users manual and program description, NASA reference publication 1311 (1996) 84–85.

[19] K. W. THOMPSON, Time dependent boundary conditions for hyperbolic systems, *Journal of Computational Physics* 68 (1) (1987) 1–24.

[20] D. H. RUDY, J. C. STRIKWERDA, A nonreflecting outflow boundary condition for subsonic navier-stokes calculations, *Journal of Computational Physics* 36 (1) (1980) 55–70.

[21] T. LU, C. K. LAW, A directed relation graph method for mechanism reduction, Proceedings of the Combustion Institute 30 (1) (2005) 1333–1341.

[22] A. MIYOSHI, KUCRS software library. see the web: http://www.frad.t.u-tokyo.ac.jp/˜miyoshi/KUCRS/ for update information. The program uses THERM program for thermodata generation.